

reactions

IMPACT
FACTOR
2.2

CITESCORE
3.3

Article

Electroreduction of Nitrogen on Pd, Rh, and PdRh Catalysts: An Online Mass Spectrometry Study


Rodrigo Gomes de Araujo, Caio Eduardo Canin de França and Joelma Perez



<https://doi.org/10.3390/reactions6030044>

Article

Electroreduction of Nitrogen on Pd, Rh, and PdRh Catalysts: An Online Mass Spectrometry Study

Rodrigo Gomes de Araujo , Caio Eduardo Canin de França and Joelma Perez *

São Carlos Institute of Chemistry, University of São Paulo, São Paulo 13560-970, Brazil;
rodridearaujo@gmail.com (R.G.d.A.); caiocanin123@alumni.com.br (C.E.C.d.F.)

* Correspondence: jperez@iqsc.usp.br

Abstract

The nitrogen electroreduction reaction (NRR) has emerged as a promising and sustainable alternative to the Haber–Bosch process for NH_3 production. This study investigated the NRR in alkaline medium using Pd/C, Rh/C, and PdRh/C electrocatalysts, employing online electrochemical mass spectrometry (OLEMS) for gaseous-product detection and ultraviolet–visible spectroscopy to confirm NH_3 formation. To our knowledge, no previous reports have simultaneously detected H_2 , N_2H , and N_2H_2 intermediates and monitored N_2 consumption as a function of applied potential for Pd and Rh catalysts. The bimetallic PdRh/C catalyst showed superior NRR performance compared with the monometallic catalysts, exhibiting higher faradaic charges, more pronounced generation of nitrogen intermediates, and selectivity for NH_3 . This work provides key insights into the NRR mechanisms and underlines the strategic importance of the bimetallic catalyst design for more efficient, sustainable electrochemical NH_3 synthesis.

Keywords: nitrogen reduction reaction (NRR); electrocatalysis; ammonia; online electrochemical mass spectrometry (OLEMS)



Academic Editor: Dmitry Yu. Murzin

Received: 30 June 2025

Revised: 6 August 2025

Accepted: 11 August 2025

Published: 12 August 2025

Citation: de Araujo, R.G.; de França, C.E.C.; Perez, J. Electroreduction of Nitrogen on Pd, Rh, and PdRh Catalysts: An Online Mass Spectrometry Study. *Reactions* **2025**, *6*, 44. <https://doi.org/10.3390/reactions6030044>

Copyright: © 2025 by the authors. Licensee MDPI, Basel, Switzerland. This article is an open access article distributed under the terms and conditions of the Creative Commons Attribution (CC BY) license (<https://creativecommons.org/licenses/by/4.0/>).

1. Introduction

Ammonia (NH_3) is a widely used compound, primarily as a source of nitrogen in fertilizers. Additionally, it stands out as a promising energy vector due to its high hydrogen content (17.8 wt.%) and high energy density (4.32 kW h L^{-1}), with annual production reaching approximately 200 million metric tons [1,2]. An alternative to the Haber–Bosch process for NH_3 production is the electroreduction of nitrogen gas (N_2) to NH_3 (the nitrogen electroreduction reaction [NRR]), which can be carried out at room temperature and atmospheric pressure. When powered by renewable energy sources, this process can avoid carbon dioxide (CO_2) emissions, offering a more sustainable pathway for NH_3 synthesis. However, the NRR faces several challenges, such as the high stability of N_2 , the low solubility of N_2 in aqueous systems (approximately 0.66 mmol L^{-1}), the slow reaction kinetics, and the hydrogen evolution reaction (HER), which competes with the NRR for the catalytic surface [3]. In aqueous systems, the HER often competes directly with the NRR, as both processes involve proton-coupled electron transfer steps. The HER tends to dominate due to its more favorable thermodynamics and faster kinetics. Compared with non-aqueous systems, which offer higher N_2 solubility and reduced HER competition [4], aqueous electrolytes have been widely used in recent NRR studies due to their practicality and alignment with environmentally friendly approaches.

Noble metal-based catalysts, such as gold (Au), platinum (Pt), ruthenium (Ru), palladium (Pd), and rhodium (Rh) [4–9], have been widely used in the NRR, primarily due to their highly active surfaces, high conductivity, and ability to form bonds with various chemical species [5]. Among these metals, Rh stands out for presenting, according to density functional theory (DFT) calculations, a predicted performance close to the top of the volcano curve, indicating high catalytic activity in the initial step of N_2 activation [6]. Furthermore, Rh-based catalysts with different morphologies and supports have been widely explored for NRR [7–12].

Zhang et al. [11] investigated the NRR by using Rh-based nanoparticles (NPs) and evaluated the effect of the support on catalytic activity. NPs supported on carbon nanotubes (CNTs) showed better performance, which was associated with the interaction between Rh NPs and CNT, with an NH_3 yield of $26.91 \mu g h^{-1} mg_{cat}^{-1}$, compared with unsupported NPs ($12 \mu g h^{-1} mg_{cat}^{-1}$) and bulk Rh ($4 \mu g h^{-1} mg_{cat}^{-1}$) at -0.1 V vs. reversible hydrogen electrode (RHE) in $0.1 mol L^{-1}$ phosphate-buffer solution (PBS).

Shen et al. [12] used single Rh atoms supported on manganese dioxide (MnO_2). The NH_3 production rate was evaluated both in diluted electrolyte ($0.1 mol L^{-1} K_2SO_4$) and in a concentrated medium of $9 mol L^{-1} K_2SO_4$, known as a water-in-salt electrolyte (WISE). The catalyst showed an NH_3 yield of $271.8 \mu g h^{-1} mg_{cat}^{-1}$ at -0.4 V vs. RHE in the WISE, significantly higher than that obtained in the diluted electrolyte ($50 \mu g h^{-1} mg_{cat}^{-1}$). The authors attributed this improved performance to the suppression of the HER provided by the solvation effects of the WISE, which favors N_2 enrichment at the catalyst active sites and consequently promotes subsequent NRR steps. In addition to NH_3 quantification, the authors investigated the interaction between N_2 and the catalytic system by using Fourier-transform infrared (FTIR) and Raman spectroscopy in the WISE, observing signals between 1100 and $1500 cm^{-1}$, attributed to N–N stretching and intermediates containing $-NH_{x,ads}$ groups (N–H stretching, $-NH_2$ wagging, and H–N–H bending, among others). Additionally, Raman spectroscopy revealed a band at approximately $480 cm^{-1}$, attributed to the formation of a Rh–N bond, indicating the adsorption and possible activation of the N_2 molecule on the catalyst surface.

Yao et al. [9] investigated the NRR on Rh surfaces using surface-enhanced infrared absorption spectroscopy (SEIRAS) and differential electrochemical mass spectrometry (DEMS) in $0.1 mol L^{-1} KOH$ as the electrolyte. SEIRAS measurements identified N_2H_x species ($0 \leq x \leq 2$), with bands between 1997 and $2036 cm^{-1}$. They observed the N=N stretching mode at approximately $2020 cm^{-1}$ in the potential range of 0.2 to -0.4 V vs. RHE. DEMS detected m/z 2 (H_2^+) and m/z 29 (N_2H^+) signals, with the latter detected due to the drag of the species by hydrogen gas (H_2) bubbles at more negative potentials. The m/z 30 ($N_2H_2^+$) and m/z 31 ($N_2H_3^+$) signals were not detected.

Another standout material for the NRR is Pd due to its ability to stabilize reaction intermediates, such as the adsorbed N_2H_{ads} species, often identified as the rate-determining step in NH_3 formation [13–15]. Despite this favorable characteristic, Pd-based catalysts generally exhibit low NH_3 production rates [16,17]. Wang et al. [16] investigated the NRR using Pd/C NPs in $0.1 mol L^{-1}$ PBS and reported an NH_3 yield of $4.5 \mu g h^{-1} mg_{cat}^{-1}$ at -0.1 V vs. RHE. Based on DFT calculations, the authors identified the formation of the adsorbed N_2H_{ads} species as the rate-limiting step in the process.

Xu et al. [13] investigated the NRR by using Pd-based catalysts, evaluating the performance of nanoporous palladium (np-Pd) and its hydride-modified form (np-PdH) in $0.1 mol L^{-1}$ PBS as the electrolyte. The np-PdH catalyst showed superior performance, with an NH_3 yield of $20.4 \mu g h^{-1} mg_{cat}^{-1}$ at -0.15 V vs. RHE, compared with np-Pd, which achieved $7.5 \mu g h^{-1} mg_{cat}^{-1}$ under the same conditions. Based on DFT calculations, the authors attributed the catalytic improvement to hydrogen doping in Pd, which favors N_2 ac-

tivation and conversion to $\text{N}_2\text{H}_{\text{ads}}$, which is generally considered the rate-limiting step [16] in NH_3 formation. The authors investigated the interaction between np-PdD and N_2 using FTIR and Raman spectroscopy. The results revealed a band at 1439 cm^{-1} , attributed to H–N–H bending, which, according to the authors, indicates NH_3 formation. Additionally, they observed three low-intensity bands at 1177, 1241, and 1325 cm^{-1} , attributed to the bending modes of the NH_2D_2^+ and NH_3D^+ intermediate species. Based on these findings, the authors suggested that deuterium atoms present in Pd-D directly participate in the formation of NH_3 . Raman spectroscopy identified a peak at 1644.4 cm^{-1} , attributed to overlapping H–N–H/H–O–H bending, whose intensity increased with reaction time, suggesting progressive NH_3 adsorption on the catalytic surface.

Yang et al. [18] recently reported the combination of Pd and Rh. They investigated the NRR by using boron-doped PdRh mesoporous nanotubes (B-PdRh MNTs) as the catalyst, evaluating their efficiency in converting N_2 to NH_3 in $0.1\text{ mol L}^{-1}\text{ Na}_2\text{SO}_4$ as the electrolyte. The authors reported a low NH_3 yield of $12\text{ }\mu\text{g h}^{-1}\text{ mg}_{\text{cat}}^{-1}$ at a potential of -0.2 V vs. RHE, but the material demonstrated high electrocatalytic stability.

Based on the studies reported to date on Rh and Pd catalysts, the NRR is predominantly associated with the associative mechanism, as supported by theoretical studies [11,13,16,19,20]. Although these theoretical models offer important insights, there is a lack of experimental evidence to confirm or refine the proposed reaction pathways on Rh and Pd surfaces. Recently, we investigated the NRR by using molybdenum disulfide (MoS_2) electrodes in an alkaline medium with both labeled and unlabeled compounds using online electrochemical mass spectrometry (OLEMS) and ultraviolet–visible (UV–Vis) spectroscopy [21]. Based on experimental data, we discarded certain reaction steps frequently proposed in DFT-based theoretical studies. Our utilization of isotopic labeling and OLEMS allowed us to identify the N_2H^+ and N_2H_2^+ species as the primary NRR intermediates, correlating NH_3 generation with N_2 consumption as a function of the applied potential. Despite these advances, experimental studies specifically focusing on Rh and Pd-based catalysts remain scarce, particularly those capable of directly identifying surface intermediates under operating conditions.

Herein, by combining OLEMS and UV–Vis spectroscopy, we analyzed Rh/C, Pd/C, and PdRh/C electrocatalysts for the NRR in an alkaline medium. We aimed to identify key intermediates and to elucidate the reaction pathways in these catalysts. We hypothesized that the association of Pd with Rh enhances NRR performance. Our findings contribute to the rational design of more efficient and sustainable electrocatalysts for NH_3 synthesis under mild conditions.

2. Materials and Methods

2.1. Polyol-Based Synthesis

The PdRh NPs were synthesized by a modified polyol method [22,23]. The synthesis was performed in a three-mouth flask equipped with a reflux column, with the addition of the precursors $\text{Pd}(\text{acac})_2$ and $\text{Rh}(\text{acac})_3$, together with 1,2-hexadecanediol and dioctyl ether as a solvent under an argon atmosphere. The mixture was heated to $290\text{ }^\circ\text{C}$ with the addition of oleic acid and oleylamine, and then refluxed for 30 min. After cooling, the NPs were purified, supported on Vulcan carbon (10 wt.%) by stirring for 12 h, vacuum-filtered, and dried at $80\text{ }^\circ\text{C}$.

2.2. Physical Characterization

The physical characterization of the electrocatalysts was carried out by X-ray diffraction (XRD, D8 Advance, Bruker, Hardtstrabe, Karlsruhe, Germany), transmission electron microscopy (TEM, JEM-2100 JEOL, Peabody, MA, USA), energy-dispersive X-ray spec-

troscopy (EDX, LEO-440, Cambridge, Cambridgeshire, UK), and thermogravimetry (TG, METTLER Toledo, Columbus, Ohio, USA). XRD measurements were performed using Cu K α radiation ($\lambda = 0.15406$ nm), with a 2θ range from 20° to 100° and a scanning rate of 1° min^{-1} . The diffraction patterns were analyzed using the Crystallographica Search-Match software (version 2.1.1.1) to identify the crystalline phases. Transmission electron micrographs were acquired at an acceleration voltage of 200 keV. Particle size distributions were determined by measuring particle diameters using the ImageJ software (version 1.4.3.x.). TG analysis was conducted under a synthetic air atmosphere with a gas flow rate of 50 mL min^{-1} , a heating rate of $10^\circ \text{ C min}^{-1}$, and a temperature range of 30 to 1000° C .

2.3. Working Electrode

The NRR was evaluated by using a gas diffusion electrode (GDE) made of carbon cloth, with a geometric area of 1.9 cm^2 , on which the catalyst was deposited. The Rh/C and Pd/C catalysts used were acquired from Fuelcell Store (Rh/C) and ETEK (Pd/C), and the PdRh/C catalyst was synthesized by using the modified polyol method. For the preparation of the working electrodes, the catalyst mass was adjusted to obtain a metal loading of 0.5 mg cm^{-2} . Subsequently, $37 \mu\text{L}$ of Nafion (5% *w/w*) and five drops of isopropyl alcohol were added to the material, which was subjected to ultrasonic bath for 15 min. Afterwards, the obtained catalytic ink was transferred to the GDE, which was dried at 80° C for 1 h.

2.4. OLEMS

The distribution of gaseous products was monitored by OLEMS, which involves the analysis of gases generated during electrochemical polarization. The equipment used was from OmniStar[®], model GSD 301 (Pfeiffer Vacuum, Frankfurt, Hesse, Germany), Prisma QMS 200, operating with an ionization energy of 70 eV, an emission current of 1 mA, and a pressure of 10^{-6} mbar. The mass spectrometer capillary was coupled to the outlet of the cathodic compartment of the electrochemical cell. The detailed scheme of the cell can be consulted in Figure S1. The monitored masses, corresponding to the gaseous products, were m/z 2, m/z 28, m/z 29, and m/z 30, attributed to the species H_2^+ , N_2^+ , N_2H^+ , and N_2H_2^+ , respectively. To ensure reproducibility, the OLEMS experiments were repeated multiple times, and the curves shown are representative of the consistent trends observed across all measurements.

2.5. Electrochemical Characterization

A bipotentiostat (PARSTAT 3000A-DX, Princeton Applied Research, Oak Ridge, TN, USA) was used for the electrochemical characterization of the electrocatalysts. For the electrochemical measurements, the catalyst was deposited on the GDE. Cyclic voltammetry was obtained in the potential range of 0.1 to 1.0 V vs. RHE, with a scan rate of 5 mV s^{-1} , in 1.0 mol L^{-1} sodium hydroxide (NaOH). Chronoamperometry coupled with mass spectrometry (CA-MS) was conducted in an H-type electrochemical cell, separated by a Nafion 115 membrane, using a Hg|HgO (1.0 mol L^{-1} NaOH) reference electrode and a graphite counter electrode (Figure S1). The dried Nafion 115 membranes were activated by immersion in a hydrogen peroxide (H_2O_2) solution (3% wt.%) at 80° C for 1 h. Then, the membranes were washed to remove any H_2O_2 residue and subjected to a similar procedure in sulfuric acid (H_2SO_4 , 0.5 mol L^{-1}) at the same temperature. Finally, the membranes were stored in Milli Q water for later use.

The measurements were performed in solutions saturated with nitrogen 6.0 (99.9999% N_2) and, as a blank, in a helium 6.0 atmosphere. The applied potentials for Rh/C, Pd/C, and PdRh/C during the CA-MS experiments were 0.0, -0.1 , -0.2 , -0.3 , -0.4 , -0.5 , and

−0.6 V vs. RHE. Between each potential step, polarization at 0.05 V vs. RHE was performed for 600 s to stabilize the catalyst surface before proceeding to the next potential.

2.6. Determination of NH_3

NH_3 was quantified with the indophenol blue method [18,24,25], in which alkaline phenol and sodium hypochlorite react with NH_3 to form the indophenol blue compound, whose concentration is proportional to the NH_3 concentration present in the solution. At the end of the polarization step, 2 mL of the solution from the cathodic compartment was collected for subsequent analysis. The absorbance measurements were performed using a UV–Vis spectrophotometer (UV-2600, Shimadzu, Malaga, Australia).

2.7. Measurement Protocol

In studies involving the NRR, Suryanto et al. [26] highlighted the difficulty of conclusively proving that the detected NH_3 results solely from the electrochemical reduction of N_2 , rather than from contamination originating from the gas feed, electrolyte, catalyst materials, or the separation membrane. To address this, NH_3 was initially quantified on the electrolytes, revealing no signs of contamination (Figure S2). Prior to polarization, the system was purged with either N_2 or He gas (blank control) for 60 min to ensure a clean environment. The Nafion 115 membrane was replaced after each experimental run.

3. Results and Discussion

3.1. Characterization of the Physical Properties

Figure 1A1 shows the XRD patterns obtained for the Rh/C, Pd/C, and PdRh/C electrocatalysts. The diffraction patterns are compatible with the Joint Committee on Powder Diffraction Standards (JCPDS) and in agreement with the materials described in the literature [27,28]. The analyses revealed that all materials exhibited a face-centered cubic (FCC) structure. For all catalysts, the peak at 24.5° on the diffractogram can be attributed to the presence of carbon. The observed peak for the Pd/C catalyst at 34° on the diffractogram can be attributed to the presence of $\text{PdO}\cdot\text{H}_2\text{O}$ [28]. TG analysis was performed on the Rh/C, Pd/C, and PdRh/C catalysts, whose mass loss curves are shown in Figure S3. The temperature range from 25 to 260°C corresponded to the removal of wastewater from the synthesis process. From 280 to 550°C , there was oxidation of the carbon carrier in the three catalysts. Above 650°C , with the stabilization of the mass, it was possible to determine the metallic content of Rh, Pd and PdRh present in the samples. TG analysis indicated metal loading of approximately 30% for Rh/C, 20% for Pd/C, and 10% for PdRh/C. EDX indicated an atomic ratio of $\text{Pd}_{55}:\text{Rh}_{45}$ for the PdRh/C catalyst, a value close to the expected nominal composition of 50:50 (Table S1).

The cyclic voltammograms of the Rh/C, Pd/C, and PdRh/C in 1.0 mol L^{-1} NaOH solution, recorded in the potential range of 0.1 to 1.0 V vs. RHE and at a scan rate of 5 mV s^{-1} , are shown in Figure 1A2. The curves show the typical electrochemical behavior of Pd and Rh [29], with regions attributed to hydrogen adsorption and absorption, as well as the formation/reduction of the metal oxide layer. The peaks observed between 0.1 and 0.4 V vs. RHE correspond to hydrogen adsorption/absorption and were used to determine the electrochemical surface area (ECSA) [30] for the Rh, Pd, and PdRh catalysts: 91.0, 56.0, and 46.0 cm^2 , respectively.

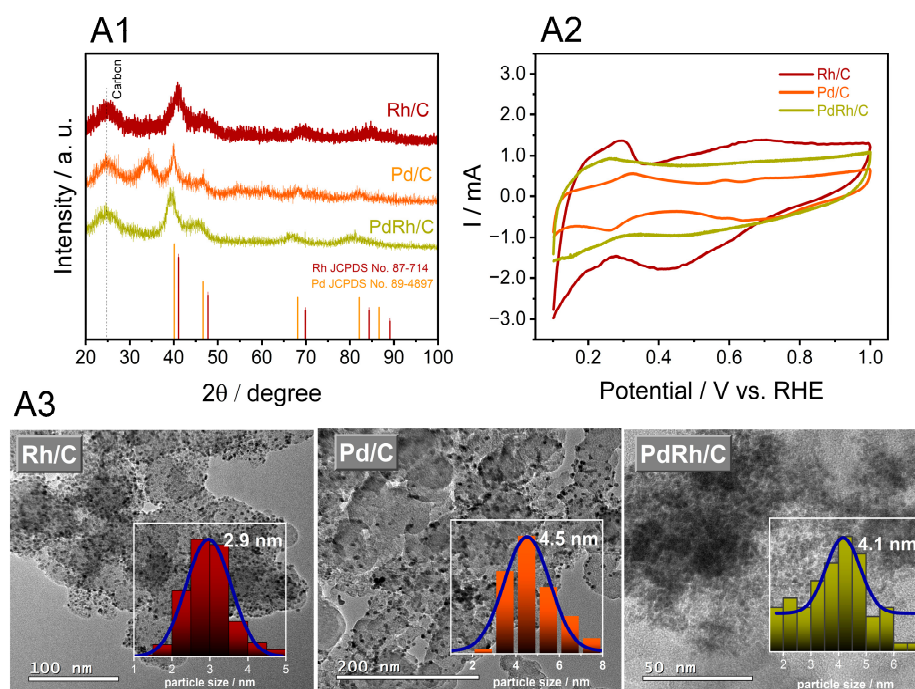


Figure 1. (A1) X-ray diffraction analysis for the Rh/C, Pd/C, and PdRh/C and Rh and Pd electrocatalysts. The Joint Committee on Powder Diffraction Standards (JCPDS) peaks are shown. (A2) Cyclic voltammograms of the Rh/C, Pd/C, and PdRh/C electrocatalysts in 1.0 mol L⁻¹ NaOH at a scan rate of 5 mV s⁻¹. (A3) Transmission electron micrographs of the Rh/C, Pd/C, and PdRh/C electrocatalysts.

The transmission electron micrographs of the electrocatalysts (Figure 1A3) revealed a predominantly spherical morphology, with a homogeneous distribution of the particles on the carbon support and no visible agglomeration. The average particle size was 2.9, 4.5, and 4.1 nm for the Rh/C, Pd/C, and PdRh/C catalysts, respectively. In electrocatalysis, particle sizes in the range of 2 to 5 nm maximize the active area. In addition, all catalysts showed good dispersion. The current was normalized by ECSA to compare the electrocatalytic activity.

3.2. Electrocatalytic NRR Performance

Figure 2 shows the CA-MS results for the Rh/C (Figure 2A), Pd/C (Figure 2B), and PdRh/C (Figure 2C) electrocatalysts. The monitored m/z signals were 2, 28, 29, and 30, corresponding to the species H₂⁺, N₂⁺, N₂H⁺, and N₂H₂⁺, respectively. For all catalysts, measurements carried out in the absence of N₂ (in a He atmosphere) are shown in blue, while the NRR-related signals are represented in wine, orange, and green for Rh, Pd, and PdRh, respectively.

The CA-MS results for the m/z 2 signal, attributed to hydrogen, are presented in Figure 2A1–C1 for Rh, Pd, and PdRh, respectively. For all catalysts, in the presence and absence of N₂, H₂ was produced, with onset at 0.0 V. Additionally, there was an increase in H₂ production as the applied potential increased, indicating that all catalysts are active for the HER.

The m/z 28 signal, attributed to nitrogen, exhibited a consumption band starting from 0.0 V vs. RHE for the Rh and PdRh catalysts (Figure 2A2,C2) and from −0.1 V for Pd (Figure 2B2), indicating anticipation for the NRR in the Rh-containing catalysts. This anticipation may indicate that the initial step of adsorption and activation of N₂ on the catalyst surface at a low potential is favored [6,12]. All materials showed an increase in consumption as the potential increased in the cathodic direction.

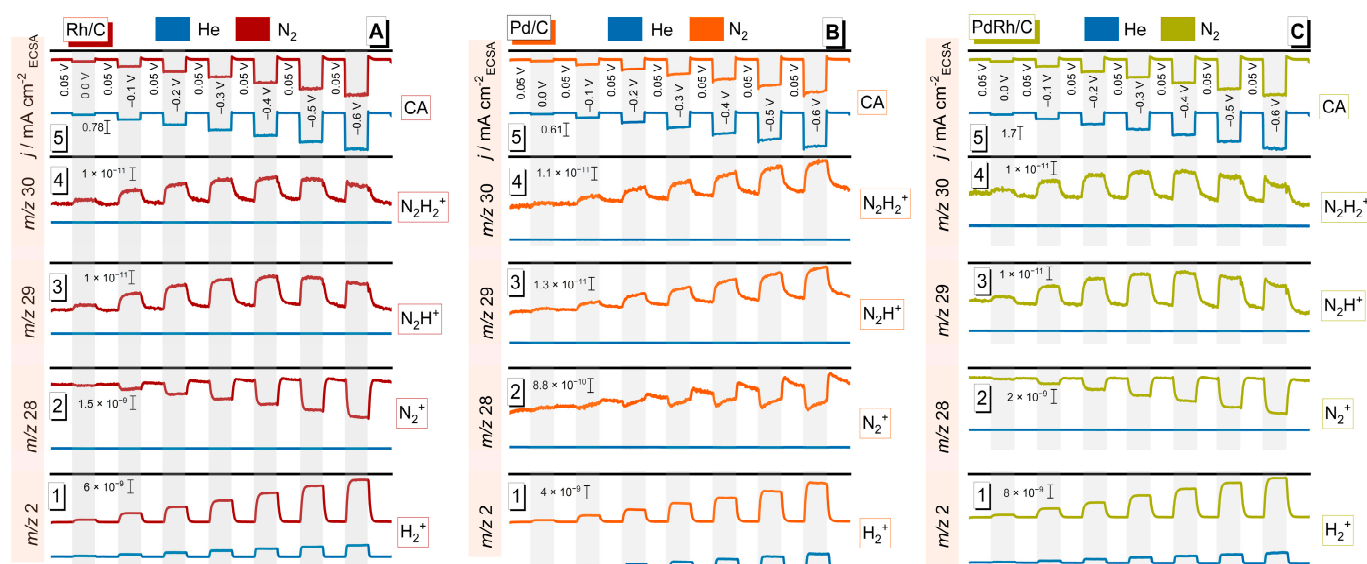


Figure 2. The CA-MS results in 1.0 mol L^{-1} NaOH for the nitrogen electroreduction reaction: (A) the Rh/C electrocatalyst (wine line), (B) the Pd/C electrocatalyst (orange line), and (C) the PdRh/C electrocatalyst (green line). The blue line indicates the helium (He) atmosphere.

The CA-MS data for the m/z 29 (N_2H^+) and m/z 30 (N_2H_2^+) signals are presented in Figure 2A3,4–C3,4 for Rh, Pd, and PdRh, respectively. Consistent with the onset of N_2 consumption, N_2H and N_2H_2 were detected starting from 0.0 V vs. RHE for Rh and PdRh and from -0.1 V vs. RHE for Pd. Yao et al. [9] detected the m/z 29 signal (N_2H^+) on Rh surfaces starting from a potential of -0.7 V vs. RHE, and they did not detect the m/z 30 signal (N_2H_2^+). Shen et al. [12] observed the adsorbed N_2 and NH_{xads} species in the FTIR spectra at a potential of -0.4 V vs. RHE for Rh_1/MnO_2 catalysts, while the Raman spectra showed a vibrational band at 480 cm^{-1} that was attributed to the Rh–N interaction.

The detection of H_2 , N_2H , and N_2H_2 , with N_2 consumption as a function of the applied potential on the Rh, Pd, and PdRh surfaces, is one of the main highlights of this work, given the scarcity of published studies that have employed coupled techniques to monitor NRR products and intermediates as a function of potential. In the absence of N_2 , the signals related to the NRR species were not detected, as expected, confirming the purity of the reagent gases, electrolytes, and system cleanliness [26].

Figure 3(1–5) present the integrated charges as a function of the applied potential for the Rh/C, Pd/C, and PdRh/C electrocatalysts, obtained from the CA and CA-MS (Figure 2A–C), to allow comparison of the electrocatalytic activity based on the OLEMS data. Among the evaluated materials, the PdRh/C catalyst, followed by Rh/C, exhibited the highest faradaic charge, suggesting enhanced electrochemical activity at the investigated potentials for both the NRR and HER.

Figure 3(2) shows an increase in the integrated charge associated with H_2 production with the application of more negative potentials, with a higher charge observed for the PdRh/C catalyst. The integrated charges associated with N_2 consumption (Figure 3(3)) also indicated greater consumption for the PdRh catalyst, followed by the Rh and Pd catalysts. These results suggest that PdRh exhibits higher activity toward both the HER and the NRR, corroborating the faradaic charge data obtained based on CA.

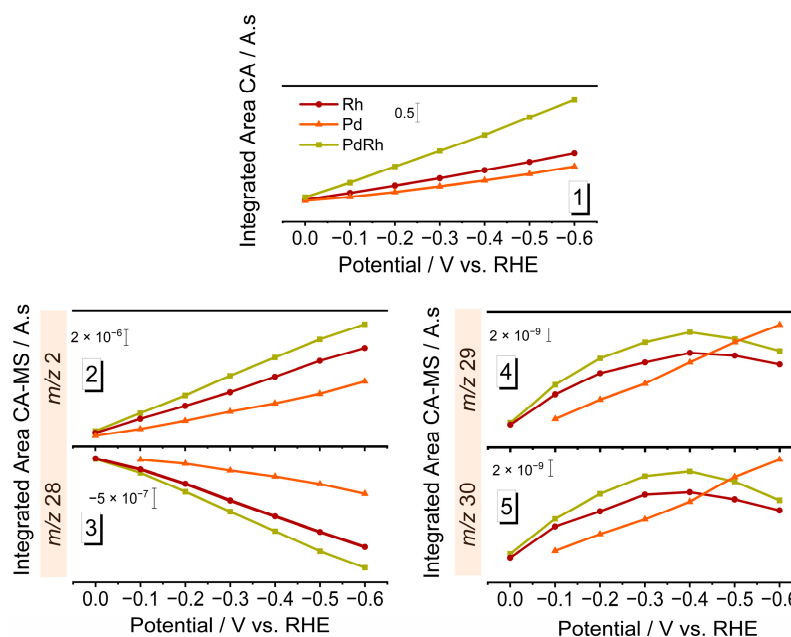


Figure 3. Integrated charge as a function of the applied potential obtained from CA-MS.

The integrated charges related to m/z 29 (N_2H^+) and m/z 30 ($N_2H_2^+$) in Figure 3(4,5), respectively, indicate the formation of NRR intermediates. For the Pd/C catalyst, the integrated charge related to the intermediate species indicated an increase in production. In this potential region, the HER competitive effect was less pronounced, likely due to the later onset of the NRR. Conversely, the Rh/C and PdRh/C catalysts exhibited similar behavior, starting at 0.0 V, with a plateau in intensity from a potential of -0.3 V, reaching its maximum value at -0.4 V, followed by a reduction in intensity up to -0.6 V vs. RHE. This trend suggests that at more negative potentials, the competition with the HER becomes more pronounced, intensifying the consumption of most of the available electrons, occupying active surface sites with adsorbed hydrogen atoms (H^*), and destabilizing nitrogen intermediates, thereby reducing the overall catalytic efficiency for NH_3 formation [16]. The production of N_2H and N_2H_2 species was also more pronounced for the PdRh catalysts between -0.3 and -0.4 V, indicating that this is the most favorable potential range for NRR.

Finally, to evaluate and confirm NH_3 production by using UV-Vis spectroscopy, CA was performed in 1.0 mol L^{-1} NaOH at a potential of -0.4 V vs. RHE for 1 h on the Rh/C, Pd/C, and PdRh/C electrocatalysts (Figure S2). The Rh/C catalyst showed NH_3 production of $26 \text{ } \mu\text{g h}^{-1} \text{ mg}_{\text{cat}}^{-1}$. These results can be compared with those obtained by Zhang et al. [11] for Rh NPs supported on CNTs (Rh/CNT) in 0.1 mol L^{-1} KOH. The authors reported a production rate of approximately $7.2 \text{ } \mu\text{g h}^{-1} \text{ mg}_{\text{cat}}^{-1}$ at a potential of -0.4 V vs. RHE, indicating that the NH_3 production obtained for Rh/C was superior at the same potential.

At -0.4 V vs. RHE, the Pd/C catalyst achieved an NH_3 yield of $3 \text{ } \mu\text{g h}^{-1} \text{ mg}_{\text{cat}}^{-1}$. Wang et al. [16] reported similar results in their investigation of the NRR using the Pd/C catalyst. They observed the highest performance at a potential of -0.05 V vs. RHE in 0.1 mol L^{-1} NaOH, with an NH_3 yield of $1 \text{ } \mu\text{g h}^{-1} \text{ mg}_{\text{cat}}^{-1}$. In another study, for np-Pd in 0.1 M PBS at -0.15 V vs. RHE, the NH_3 yield was $7.5 \text{ } \mu\text{g h}^{-1} \text{ mg}_{\text{cat}}^{-1}$ [13].

The PdRh/C electrocatalyst had an NH_3 yield of $64 \text{ } \mu\text{g h}^{-1} \text{ mg}_{\text{cat}}^{-1}$ at -0.4 V vs. RHE. This is notably higher than the yield of $12 \text{ } \mu\text{g h}^{-1} \text{ mg}_{\text{cat}}^{-1}$ reported for boron-doped PdRh mesoporous nanotubes at -0.2 V vs. RHE in 0.1 mol L^{-1} Na_2SO_4 [18].

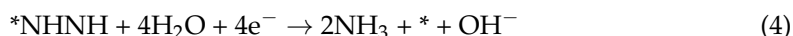
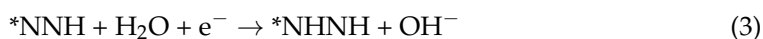
The NH_3 faradaic efficiency for all catalysts at a potential of -0.4 V vs. RHE presented the order PdRh/C (5.7%) > Rh/C (4.9%) > Pd/C (0.9%), which corroborates the results

obtained for CA-MS (Figure 3(3–5)). The superior performance of the Rh and PdRh catalysts, associated with the reduction in the NRR onset potential compared with the Pd/C catalyst, observed with the OLEMS results for intermediate species at low potentials, is consistent with reports indicating high catalytic activity in the initial step of $\text{N}\equiv\text{N}$ bond weakening [15]. The Pd/C electrocatalyst exhibited limited faradaic efficiency, consistent with the literature [31], despite its ability to stabilize key intermediates during the NRR ($^*\text{N}_2\text{H}_x$) [13,16], likely due to competition with the HER.

In summary, the combination of Pd and Rh enhanced NRR activity: Rh serves as the primary site for N_2 adsorption and activation, while Pd facilitates proton transfer and provides reactive hydrogen species ($^*\text{H}$) for intermediate hydrogenation steps. Additionally, electronic interactions between Pd and Rh can modify the adsorption energies of intermediates, thereby optimizing both activation and desorption processes [6,7,10,12,15]. Thus, the Pd–Rh bimetallic system represents a promising approach for developing efficient and selective NRR electrocatalysts.

It was possible to qualitatively identify the formation of N_2H and N_2H_2 , as well as the consumption of N_2 , under the applied potential, and the resulting NH_3 production. The combination of Rh and Pd decreased the onset of the reaction and led to a gain in catalytic activity based on OLEMS and UV–Vis spectroscopy.

Although there is an ongoing debate regarding the active species in the NRR, N_2Hy intermediates ($1 \leq y \leq 2$) are frequently identified as crucial in NH_3 formation. In this study, (i) N_2H^+ and N_2H_2^+ were detected as intermediates beginning at 0.0 V vs. RHE for the Rh and PdRh electrocatalysts, and beginning at -0.1 V vs. RHE for the Pd electrocatalyst. (ii) N_2 consumption began at 0.0 V vs. RHE for the Rh and PdRh electrocatalysts, and at -0.1 V vs. RHE for the Pd electrocatalyst. (iii) UV–Vis spectroscopy confirmed the presence of NH_3 . (iv) There were no signals corresponding to N_2H_3^+ or N_2H_4^+ . Moreover, our earlier isotopic labeling experiments supported these findings, showing no trace of N_2H_3^+ or N_2H_4^+ , and further confirming the absence of N_2H_4 based on UV–Vis spectroscopy [21]. Based on these data, we propose a plausible NRR mechanism occurring on the Pd, Rh, and PdRh electrocatalyst surfaces, as outlined in reactions 1 to 4. In this pathway, N_2 molecules adsorb onto the catalyst and undergo two successive protonation steps, forming N_2H and N_2H_2 at an electrode potential below 0.0 V for the Rh and PdRh electrocatalysts and below -0.1 V for the Pd electrocatalyst. Among these, we suggest that N_2H_2 is the principal intermediate responsible for NH_3 generation.



*Active site.

4. Conclusions

We demonstrated the effectiveness of combining OLEMS and UV–Vis spectroscopy to investigate the Rh/C, Pd/C, and PdRh/C electrocatalysts for the NRR in an alkaline medium. The simultaneous detection, unprecedented to our knowledge, of the intermediates N_2H^+ and N_2H_2^+ , as well as the observation of N_2 consumption as a function of the applied potential for these materials, represents a significant advance in elucidating the NRR pathways. The PdRh/C catalyst demonstrated superior electrocatalytic performance, especially at low potentials, showing higher faradaic charges and enhanced formation of

nitrogen-related intermediates. Nonetheless, at more negative potentials, competition with the HER intensifies, reducing the number of active catalytic sites and compromising the stability of nitrogen intermediates. At -0.4 V vs. RHE, PdRh/C achieved the highest NH_3 faradaic efficiency among the evaluated electrocatalysts, outperforming both Rh/C and Pd/C, as supported by the CA-MS and OLEMS data. This enhanced activity is attributed to the bifunctional and electronic effects between Rh and Pd: Rh promotes N_2 adsorption and activation, while Pd facilitates hydrogenation steps. Their electronic interaction contributes to the optimization of adsorption energies and reaction kinetics. All tested catalysts followed a mechanism in which N_2 is initially adsorbed onto the surface, followed by successive protonation steps, with N_2H and N_2H_2 acting as key intermediates in the formation of NH_3 . The combination of Rh and Pd yields a bimetallic catalyst with synergistic properties, facilitating improved nitrogen activation and enhanced electrochemical performance. These findings underscore the potential of bimetallic systems in advancing efficient and sustainable NH_3 synthesis via electrochemical routes.

Supplementary Materials: The following supporting information can be downloaded at: <https://www.mdpi.com/article/10.3390/reactions6030044/s1>, Reagents; NH_3 yield; Figure S1: Electrochemical cell; Figure S2: (a) Calibration curve used for calculation of NH_4^+ concentrations in 1 mol L^{-1} NaOH. (b) Quantification of NH_4^+ at potentials of -0.4 V for Rh/C, Pd/C, and PdRh/C catalysts; Figure S3: TGA analysis for Rh/C, Pd/C, and PdRh/C catalysts; Table S1: EDS analysis of the PdRh/C catalyst.

Author Contributions: Conceptualization, R.G.d.A., C.E.C.d.F., and J.P.; methodology, R.G.d.A., C.E.C.d.F., and J.P.; software, R.G.d.A.; validation, R.G.d.A., C.E.C.d.F., and J.P.; formal analysis, R.G.d.A., C.E.C.d.F., and J.P.; investigation, R.G.d.A. and C.E.C.d.F.; resources, J.P.; data curation, R.G.d.A., C.E.C.d.F., and J.P.; writing—original draft preparation, R.G.d.A., C.E.C.d.F., and J.P.; writing—review and editing, R.G.d.A. and J.P.; visualization, R.G.d.A. and J.P.; supervision, J.P.; project administration, J.P.; funding acquisition, J.P. All authors have read and agreed to the published version of the manuscript.

Funding: The authors wish to thank the Fundação de Amparo à Pesquisa do Estado de São Paulo (FAPESP) (grant numbers 2019/22183-6 and 2024/05966-5) and the Conselho Nacional de Desenvolvimento Científico e Tecnológico (CNPq) (grant number 142482/2019-6) for their support.

Data Availability Statement: Data are available from the corresponding author upon reasonable request.

Conflicts of Interest: The authors declare no conflicts of interest.

References

1. Qing, G.; Ghazfar, R.; Jackowski, S.T.; Habibzadeh, F.; Ashtiani, M.M.; Chen, C.-P.; Smith, M.R., III; Hamann, T.W. Recent Advances and Challenges of Electrocatalytic N_2 Reduction to Ammonia. *Chem. Rev.* **2020**, *120*, 5437–5516. [\[CrossRef\]](#)
2. Nayak-Luke, R.; Bañares-Alcántara, R.; Wilkinson, I. “Green” Ammonia: Impact of Renewable Energy Intermittency on Plant Sizing and Levelized Cost of Ammonia. *Ind. Eng. Chem. Res.* **2018**, *57*, 14607–14616. [\[CrossRef\]](#)
3. Tang, C.; Qiao, S.-Z. How to explore ambient electrocatalytic nitrogen reduction reliably and insightfully. *Chem. Soc. Rev.* **2019**, *48*, 3166–3180. [\[CrossRef\]](#)
4. Bi, W.; Shaigan, N.; Malek, A.; Fatih, K.; Gyenge, E.; Wilkinson, D.P. Strategies in cell design and operation for the electrosynthesis of ammonia: Status and prospects. *Energy Environ. Sci.* **2022**, *15*, 2259–2287. [\[CrossRef\]](#)
5. Guo, X.; Du, H.; Qu, F.; Li, J. Recent progress in electrocatalytic nitrogen reduction. *J. Mater. Chem. A* **2019**, *7*, 3531–3543. [\[CrossRef\]](#)
6. Skúlason, E.; Bligaard, T.; Gudmundsdóttir, S.; Studt, F.; Rossmeisl, J.; Abild-Pedersen, F.; Vegge, T.; Jónsson, H.; Nørskov, J.K. A theoretical evaluation of possible transition metal electro-catalysts for N_2 reduction. *Phys. Chem. Chem. Phys.* **2012**, *14*, 1235–1245. [\[CrossRef\]](#)
7. Liu, H.; Han, S.; Zhao, Y.; Zhu, Y.; Tian, X.; Zeng, J.; Jiang, J.; Xia, B.; Chen, Y. Surfactant-free atomically ultrathin rhodium nanosheet nanoassemblies for efficient nitrogen electroreduction. *J. Mater. Chem. A* **2018**, *6*, 3211–3217. [\[CrossRef\]](#)
8. Wang, J.; Huang, B.; Ji, Y.; Sun, M.; Wu, T.; Yin, R.; Zhu, X.; Li, Y.; Shao, Q.; Huang, X. A General Strategy to Glassy M-Te (M = Ru, Rh, Ir) Porous Nanorods for Efficient Electrochemical N_2 Fixation. *Adv. Mater.* **2020**, *32*, 1907112. [\[CrossRef\]](#)

9. Yao, Y.; Zhu, S.; Wang, H.; Li, H.; Shao, M. A spectroscopic study of electrochemical nitrogen and nitrate reduction on rhodium surfaces. *Angew. Chem.* **2020**, *132*, 10565–10569. [[CrossRef](#)]
10. Chen, T.; Liu, S.; Ying, H.; Li, Z.; Hao, J. Reactive Ionic Liquid Enables the Construction of 3D Rh Particles with Nanowire Subunits for Electrocatalytic Nitrogen Reduction. *Chem.—Asian J.* **2020**, *15*, 1081–1087. [[CrossRef](#)]
11. Zhang, Y.; Zhang, Q.; Liu, D.-X.; Wen, Z.; Yao, J.-X.; Shi, M.-M.; Zhu, Y.-F.; Yan, J.-M.; Jiang, Q. High spin polarization ultrafine Rh nanoparticles on CNT for efficient electrochemical N₂ fixation to ammonia. *Appl. Catal. B Environ.* **2021**, *298*, 120592. [[CrossRef](#)]
12. Shen, P.; Li, X.; Luo, Y.; Zhang, N.; Zhao, X.; Chu, K. Ultra-efficient N₂ electroreduction achieved over a rhodium single-atom catalyst (Rh₁/MnO₂) in water-in-salt electrolyte. *Appl. Catal. B Environ.* **2022**, *316*, 121651. [[CrossRef](#)]
13. Xu, W.; Fan, G.; Chen, J.; Li, J.; Zhang, L.; Zhu, S.; Su, X.; Cheng, F.; Chen, J. Nanoporous Palladium Hydride for Electrocatalytic N₂ Reduction under Ambient Conditions. *Angew. Chem. Int. Ed.* **2020**, *59*, 3511–3516. [[CrossRef](#)] [[PubMed](#)]
14. Montoya, J.H.; Tsai, C.; Vojvodic, A.; Nørskov, J.K. The Challenge of Electrochemical Ammonia Synthesis: A New Perspective on the Role of Nitrogen Scaling Relations. *ChemSusChem* **2015**, *8*, 2180–2186. [[CrossRef](#)]
15. Assad, S.; Tariq, T.; Zaeem Idrees, M.; Mannan Butt, A.; Bakhat, K.; Shamraiz, U. Recent progress in Pd based electrocatalysts for electrochemical nitrogen reduction to ammonia. *J. Electroanal. Chem.* **2023**, *931*, 117174. [[CrossRef](#)]
16. Wang, J.; Yu, L.; Hu, L.; Chen, G.; Xin, H.; Feng, X. Ambient ammonia synthesis via palladium-catalyzed electrohydrogenation of dinitrogen at low overpotential. *Nat. Commun.* **2018**, *9*, 1795. [[CrossRef](#)]
17. Liu, S.; Wang, Z.; Zhang, H.; Wang, S.; Wang, P.; Xu, Y.; Li, X.; Wang, L.; Wang, H. Palladium Nanothorn Assembly Array for Efficient Electroreduction of Nitrogen to Ammonia. *ACS Sustain. Chem. Eng.* **2020**, *8*, 14228–14233. [[CrossRef](#)]
18. Yang, G.; Zhang, H.; Li, J.; Wang, Y.; Deng, K.; Yu, H.; Wang, H.; Wang, Z.; Wang, L. Boron-Doped PdRh Mesoporous Nanotubes for Electrocatalytic Nitrogen Reduction to Ammonia. *ACS Appl. Nano Mater.* **2024**, *7*, 10895–10901. [[CrossRef](#)]
19. Shipman, M.; Symes, M. Recent progress towards the electrosynthesis of ammonia from sustainable resources. *Catal. Today* **2017**, *286*, 57–68. [[CrossRef](#)]
20. Cui, X.; Tang, C.; Zhang, Q. A Review of Electrocatalytic Reduction of Dinitrogen to Ammonia under Ambient Conditions. *Adv. Energy Mater.* **2018**, *8*, 1800369. [[CrossRef](#)]
21. de Araujo, R.G.; Perez, J. Nitrogen Electrochemical Reduction Reaction Pathways Evidenced by Online Electrochemical Mass Spectrometry and Isotope Labeling on the MoS₂ Surface. *ACS Electrochem.* **2025**, *1*, 294–302. [[CrossRef](#)]
22. Santiago, E.I.; Varanda, L.C.; Villullas, H.M. Carbon-Supported Pt–Co Catalysts Prepared by a Modified Polyol Process as Cathodes for PEM Fuel Cells. *J. Phys. Chem. C* **2007**, *111*, 3146–3151. [[CrossRef](#)]
23. Fievet, F.; Lagier, J.P.; Figlarz, M. Preparing Monodisperse Metal Powders in Micrometer and Submicrometer Sizes by the Polyol Process. *MRS Bull.* **1989**, *14*, 29–34. [[CrossRef](#)]
24. Aminot, A.; Kirkwood, D.S.; K  rouel, R. Determination of ammonia in seawater by the indophenol-blue method: Evaluation of the ICES NUTS I/C 5 questionnaire. *Mar. Chem.* **1997**, *56*, 59–75. [[CrossRef](#)]
25. Biswas, A.; Ghosh, B.; Dey, R.S. Refining the Spectroscopic Detection Technique: A Pivot in the Electrochemical Ammonia Synthesis. *Langmuir* **2023**, *39*, 3810–3820. [[CrossRef](#)]
26. Suryanto, B.H.R.; Du, H.-L.; Wang, D.; Chen, J.; Simonov, A.N.; Macfarlane, D.R. Challenges and prospects in the catalysis of electroreduction of nitrogen to ammonia. *Nat. Catal.* **2019**, *2*, 290–296. [[CrossRef](#)]
27. Wang, H.; Abru  a, H.D. Rh and Rh Alloy Nanoparticles as Highly Active H₂ Oxidation Catalysts for Alkaline Fuel Cells. *ACS Catal.* **2019**, *9*, 5057–5062. [[CrossRef](#)]
28. Dector, A.; Cuevas-Mu  iz, F.M.; Guerra-Balc  azar, M.; God  nez, L.A.; Ledesma-Garc  a, J.; Arriaga, L.G. Glycerol oxidation in a microfluidic fuel cell using Pd/C and Pd/MWCNT anodes electrodes. *Int. J. Hydrogen Energy* **2013**, *38*, 12617–12622. [[CrossRef](#)]
29. Jurzinsky, T.; B  r, R.; Cremers, C.; T  bke, J.; Elsner, P. Highly active carbon supported palladium-rhodium PdXRh/C catalysts for methanol electrooxidation in alkaline media and their performance in anion exchange direct methanol fuel cells (AEM-DMFCs). *Electrochim. Acta* **2015**, *176*, 1191–1201. [[CrossRef](#)]
30. Sharma, R.; Gyergyek, S.; Andersen, S.M. Critical thinking on baseline corrections for electrochemical surface area (ECSA) determination of Pt/C through H-adsorption/H-desorption regions of a cyclic voltammogram. *Appl. Catal. B Environ.* **2022**, *311*, 121351. [[CrossRef](#)]
31. Wen, Y.; Wang, T.; Hao, J.; Zhuang, Z.; Gao, G.; Lai, F.; Lu, S.; Wang, X.; Kang, Q.; Wu, G.; et al. A Coherent Pd–Pd₁₆B₃ Core–Shell Electrocatalyst for Controlled Hydrogenation in Nitrogen Reduction Reaction. *Adv. Funct. Mater.* **2024**, *34*, 2400849. [[CrossRef](#)]

Disclaimer/Publisher’s Note: The statements, opinions and data contained in all publications are solely those of the individual author(s) and contributor(s) and not of MDPI and/or the editor(s). MDPI and/or the editor(s) disclaim responsibility for any injury to people or property resulting from any ideas, methods, instructions or products referred to in the content.